

Lithium Batteries

Olefin-Linked Covalent Organic Frameworks with Electronegative Channels as Cationic Highways for Sustainable Lithium Metal Battery Anodes

Zhongping Li, Linhai Sun, Lipeng Zhai,* Kyeong-Seok Oh, Jeong-Min Seo, Changqing Li, Diandian Han,* Jong-Beom Baek, and Sang-Young Lee*

Abstract: Despite the enormous interest in Li metal as an ideal anode material, the uncontrollable Li dendrite growth and unstable solid electrolyte interphase have plagued its practical application. These limitations can be attributed to the sluggish and uneven Li^+ migration towards Li metal surface. Here, we report olefin-linked covalent organic frameworks (COFs) with electronegative channels for facilitating selective Li^+ transport. The triazine rings and fluorinated groups of the COFs are introduced as electron-rich sites capable of enhancing salt dissociation and guiding uniform Li^+ flux within the channels, resulting in a high Li^+ transference number (0.85) and high ionic conductivity (1.78 mS cm^{-1}). The COFs are mixed with a polymeric binder to form mixed matrix membranes. These membranes enable reliable Li plating/stripping cyclability over 700 h in Li/Li symmetric cells and stable capacity retention in Li/LiFePO₄ cells, demonstrating its potential as a viable cationic highway for accelerating Li^+ conduction.

Introduction

The growing demand for high-energy-density rechargeable batteries for electronics, electric vehicles, and smart grid storage has triggered the search for alternatives to cathodes and graphitic anodes, which have unfortunately reached

their capacity limits.^[1–5] Accordingly, Li metal anode has been identified as a promising solution owing to its high theoretical specific capacity ($\sim 3860 \text{ mAh g}^{-1}$) and low electrochemical potential ($\sim -3.04 \text{ V}$).^[6–8] In addition, owing to these advantages, Li metal batteries (LMBs) can achieve an energy density of 500 Wh kg^{-1} , indicating that they can fulfill the industrial requirements for practical applications in electric vehicles and grid-scale energy storage systems.^[9–11]

However, the vigorous reactivity of Li metal with electrolytes is a major challenge in achieving the high-energy-density target. To stabilize Li metal anodes, it is essential to form a stable solid-electrolyte interphase (SEI).^[12–14] However, the SEI layer is fragile and susceptible to fracture, causing undesired side reactions and Li dendrite growth, which result in poor Coulombic efficiency and internal short circuit failures.^[15–16]

Numerous approaches have been implemented to address the aforementioned issues, including new electrolytes design, artificial SEI, Li hosts, and functional separator membranes.^[17–23] Among these approaches, the use of covalent organic frameworks (COFs) in Li protective layers and single-ion conducting electrolytes has been investigated.^[24–28] COFs are a class of porous crystalline polymers, in which organic structural units are finely integrated into an ordered two-dimensional (2D) planar structure with atomic precision through covalent bonding.^[29–43] COFs are known to consist of lightweight elements (such as C, H, O, F, and N), resulting in low weights comparable to those of commercial separators.^[44] Thus, they can be suggested as promising alternative separator without impairing gravimetric energy densities of the resulting batteries. As the unstable Li plating/stripping behavior is mainly due to the sluggish and uneven Li^+ migration towards the Li metal anodes, COFs can be considered as a promising platform for enabling selective Li^+ conduction via their customized ion-conducting channels.^[45]

To achieve this goal, herein, we present olefin-linked COFs with electronegative one-dimensional (1D) channels. Triazine rings and fluorinated groups were incorporated into the COF skeletons to serve as electron-rich sites capable of having electrostatic interaction with electrolytes impregnated in the channels, thereby promoting the dissociation of salt to generate Li^+ and counter anions, and guiding uniform Li^+ flux within the channels. To gain a mechanistic understanding of the effects of COF, we synthesized a series of

[*] Dr. Z. Li, K.-S. Oh, Prof. S.-Y. Lee
Department of Chemical and Biomolecular Engineering, Yonsei University
Seoul 03722 (Republic of Korea)
E-mail: syleek@yonsei.ac.kr
L. Sun, Prof. L. Zhai, Dr. D. Han
Henan Key Laboratory of Functional Salt Materials, Center for Advanced Materials Research, Zhongyuan University of Technology
Zhengzhou 45007 (P. R. China)
E-mail: zhailp@zut.edu.cn
6788@zut.edu.cn
Dr. Z. Li, Dr. J.-M. Seo, C. Li, Prof. J.-B. Baek
School of Energy and Chemical Engineering/Center for Dimension-Controllable Organic Frameworks, Ulsan National Institute of Science and Technology (UNIST)
Ulsan 44919 (Republic of Korea)

COFs by varying the number of fluorine atoms in the olefin linkage, thus manipulating the electronegativity of the channels.

Thereafter, the COFs were mixed with polytetrafluoroethylene (PTFE) binder to produce mixed matrix membranes that can act as separator membranes when placed between electrodes. Under an optimal electronegativity environment, the COF membrane exhibited a high Li^+ transference number (t_{Li^+}) of 0.85 and high ionic conductivity of 1.78 mS cm^{-1} at room temperature, demonstrating its role as a class of cationic highway for accelerating Li^+ transport. Owing to this beneficial effect, the COF membrane enabled reliable Li plating/stripping cyclability for over 700 h in Li/Li symmetric cells. Furthermore, the COF membrane enabled a Li/LiFePO₄ cell to achieve stable capacity retention, verifying its potential as a cationic highway membrane for Li metal cells.

Results and Discussion

Three electronegativity-adjustable COFs (0F-COF, 1F-COF, and 2F-COF) with olefin linkage were synthesized using 2,4,6-trimethyl-1,3,5-triazine (TM) as the knot and terephthalaldehyde (TA), 2-fluoroterephthalaldehyde (FP), and 2,5-difluoro-1,4-benzenedialdehyde (FB) as the linker via Knoevenagel condensation (Figure 1a). The distribution of the electronegative walls increased with an increase in the number of fluorine atoms in the skeleton (Figure 1b). The chemical structures of these COFs were characterized using Fourier transform infrared (FT-IR) spectra and solid-state ^{13}C cross-polarization magic angle spinning nuclear magnetic resonance (CP/MAS NMR) spectra. Newly formed peaks were observed in the FT-IR spectra at 1624 and 993 cm^{-1} , which were assigned to the stretching vibration of trans C=C linkages (Figure S1). Further, the peaks attributed to the C=O stretching band at 1691 cm^{-1} disappeared in the FT-IR spectra of the COFs at high polymerization degrees. In addition, an intense peak was observed in the FT-IR spectra of 1F-COF and 2F-COF at approximately 1250 cm^{-1} , which was assigned to the C–F bonds, indicating that the fluorinated groups were retained after the Knoevenagel condensation. The characteristic signals of the carbons observed in the solid state ^{13}C CP/MAS NMR spectra of these COFs were assigned to their corresponding chemical structures (Figure S2–S4). The peaks observed at approximately 155 and 125 ppm were attributed to the carbons of the olefin linkages, further confirming the successful Knoevenagel condensation in these COFs. In addition, the signals observed at approximately 171 ppm were attributed to the carbons of triazine units in these COFs. The peaks observed at approximately 176 ppm in the spectra of 1F-COF and 2F-COF were assigned to the carbons of C–F bonds, further confirming that the fluorinated groups were retained in the COFs networks after polymerization (Figure S3 and S4). Thermogravimetric analysis (TGA) revealed that these COFs exhibited a good stability under nitrogen atmosphere (Figure S5). Elemental analysis revealed that the elemental contents in these COFs were consistent with the theoretical

values calculated using the frameworks (Table S1). The morphology of the as-synthesized COFs was investigated using field emission scanning electron microscopy (FE-SEM). The FE-SEM image revealed that 0F-COF and 1F-COF exhibited a uniform fiber-like morphology, whereas 2F-COF contained irregular nanoparticles (Figure S6).

The crystalline frameworks of these COFs were investigated using powder X-ray diffraction (PXRD) measurement. Four distinct peaks were observed in the PXRD pattern of the 0F-COF at 4.91, 8.40, 12.81, and 26.66°, which were assigned to the 100, 110, 210, and 001 facets, respectively (Figure 1c). In addition, peaks were observed in the PXRD pattern of 1F-COF at 4.86, 8.48, 13.56, and 25.58°, which can be assigned to the 100, 200, 300, and 001 facets, respectively (Figure 1c), and at 4.59, 6.10, 12.68, and 25.67° in the PXRD pattern of the 2F-COF, which can be assigned to the 100, 110, 220, and 001 facets, respectively (Figure 1c). The corresponding theoretical structures were reconstructed by Pawley refinements using the self-consistent charge density functional tight binding (SCC-DFTB) method. As shown in Figure 1c, the difference (black curves) between the PXRD curves calculated from Pawley refinement and the experimental PXRD profiles of all the COFs is negligible, indicating that these COFs adopted the AA stacking mode. The 0F-COF (5.88 % for R_{wp} and 4.58 % for R_{p}) exhibited a hexagonal unit cell (P6/m) with parameters of $a=b=21.3258 \text{ \AA}$, $c=3.3776 \text{ \AA}$, $\alpha=\gamma=90^\circ$, and $\beta=120^\circ$; the 1F-COF (4.98 % for R_{wp} and 3.81 % for R_{p}) exhibited a hexagonal unit cell (P6) with parameters of $a=b=28.8 \text{ \AA}$, $c=3.4079 \text{ \AA}$, $\alpha=\gamma=90^\circ$, and $\beta=120^\circ$; and the 2F-COF (3.90 % for R_{wp} and 3.03 % for R_{p}) exhibited a hexagonal unit cell (P6/m) with parameters of $a=b=22.0880 \text{ \AA}$, $c=3.4614 \text{ \AA}$, $\alpha=\gamma=90^\circ$, and $\beta=120^\circ$. In contrast, the differences between the PXRD profiles generated from the staggered (AB) stacking mode and the experimental patterns of these COFs were significant (Figure 1c, cyan curve).

The nitrogen adsorption isotherms were measured at 77 K to investigate the intrinsic porosity of these COFs. All the COFs exhibited the typical type-I N_2 sorption isotherms, indicating that they exhibited microporous structures (Figure 1d). The Brunauer–Emmett–Teller (BET) surface area of the 0F-COF, 1F-COF, and 2F-COF was 911, 806, and 871 $\text{m}^2 \text{ g}^{-1}$, respectively. The pore size distribution calculated using the density functional theory (DFT) model demonstrated that the pore size of 0F-COF, 1F-COF, and 2F-COF were centered at 1.2 nm (Figure S7).

The as-synthesized electronegative COFs were mixed with PTFE binder to fabricate mixed matrix membranes that can act as Li^+ flux-enhancing separator membranes between electrodes. The FE-SEM images of the mixed matrix membranes revealed that the COFs were uniformly distributed in the through-thickness direction of the membrane (Figure S8). The resulting COF membrane exhibited high flexibility with a thickness of 80 μm . To prepare the electrolytes to be impregnated in the COF channels, lithium bis-trifluoromethanesulfonimide (LiTFSI) was dissolved in a solvent mixture (fluoroethylene carbonate (FEC)/succinonitrile (SN)=1/20 (weight ratio)) at a molar ratio of LiTFSI/

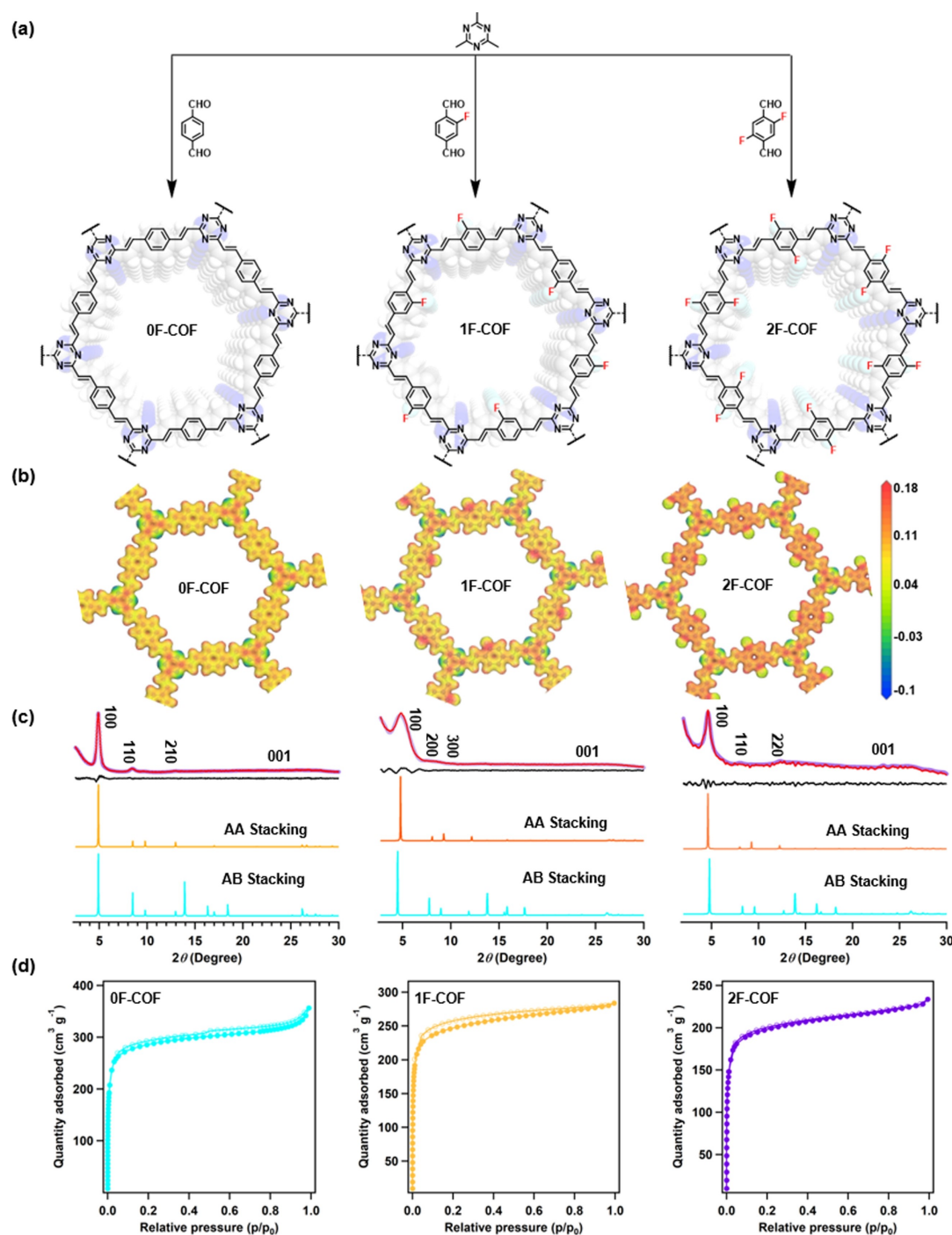


Figure 1. (a) Schematic synthesis route of COFs. (b) Electrostatic potential (ESP)-mapped surface of 0F-COF, 1F-COF, and 2F-COF. (c) PXRD patterns of 0F-COF, 1F-COF, and 2F-COF: experimental (red), Pawley-refine (purple), simulated powder X-ray diffraction patterns of AA (orange) and AB (cyan) stacking, and difference curves (black). (d) N₂ adsorption-desorption isotherms of 0F-COF, 1F-COF, and 2F-COF under 77 K.

SN=1/20. Many previous studies reported the use of FEC/SN electrolytes in Li batteries.^[46–49] They demonstrated that the addition of FEC into SN mitigated the SN-triggered interfacial side reactions with the Li metal anode and the resulting FEC/SN electrolyte allowed for the stable electrochemical performance of the Li batteries. Thereafter, the as-prepared electrolyte (LiTFSI-SN/FEC) was impregnated into the COF membranes after storage at 60 °C for 12 h. The

cross-sectional FE-SEM and corresponding energy dispersive spectroscopy (EDS) mapping images revealed that the electrolyte was successfully embedded inside the porous channels of the COF membranes, thus enabling ion transport across the electrolyte-filled COF membranes (hereinafter, denoted as EL-COF membranes; Figure S9).

The EL-COF membranes with different numbers of fluorine atoms in the skeletons exhibited a good flexibility

(Figure 2a–c). This mechanical flexibility of the EL-COF membranes was further verified by quantitatively analyzing their tensile stress-strain behavior (Figure S10). The mechanical strength values of the 0F-COF, 1F-COF, and 2F-COF membranes were estimated to be 2.23, 3.11, and 3.63 MPa, respectively. The higher tensile strength of the 2F-COF membrane compared to other COF membranes may be due to higher fluorine content. The ionic conductivities of the EL-COF membranes tended to increase in the order of 0F-COF (1.12 mS cm^{-1}) < 1F-COF (1.49 mS cm^{-1}) < 2F-COF (1.78 mS cm^{-1} ; Figure 2d), and were higher than that of a control sample (electrolyte-filled glass fiber (GF) and PTFE membrane) (Figure S11). This result indicated the superiority of the EL-COF membranes in facilitating Li^+ conduction. Particularly, 2F-COF exhibited the highest ionic conductivity, indicating that it contained the highest number

density of fluorine atoms, which contributed to the facilitation of Li^+ conduction.

In addition to the ionic conductivity, the Li^+ transference number (t_+) of the EL-COF membranes was investigated using direct current (DC) polarization and AC impedance methods with Li/Li symmetric cells (Figure 2e and Figure S12). It should be noted that the low t_+ of electrolytes tends to result in the accumulation of large Li^+ concentration gradient on the surface of Li metal anodes, resulting in a strong interfacial electric field and acceleration of dendrite propagation. The estimated t_+ values of the 0F-COF, 1F-COF, and 2F-COF were 0.72, 0.80, and 0.85, respectively, which were significantly higher than that of the GF membrane (0.36) and PTFE membrane (0.30) (Figure S11c). The higher t_+ values of the EL-COF membranes

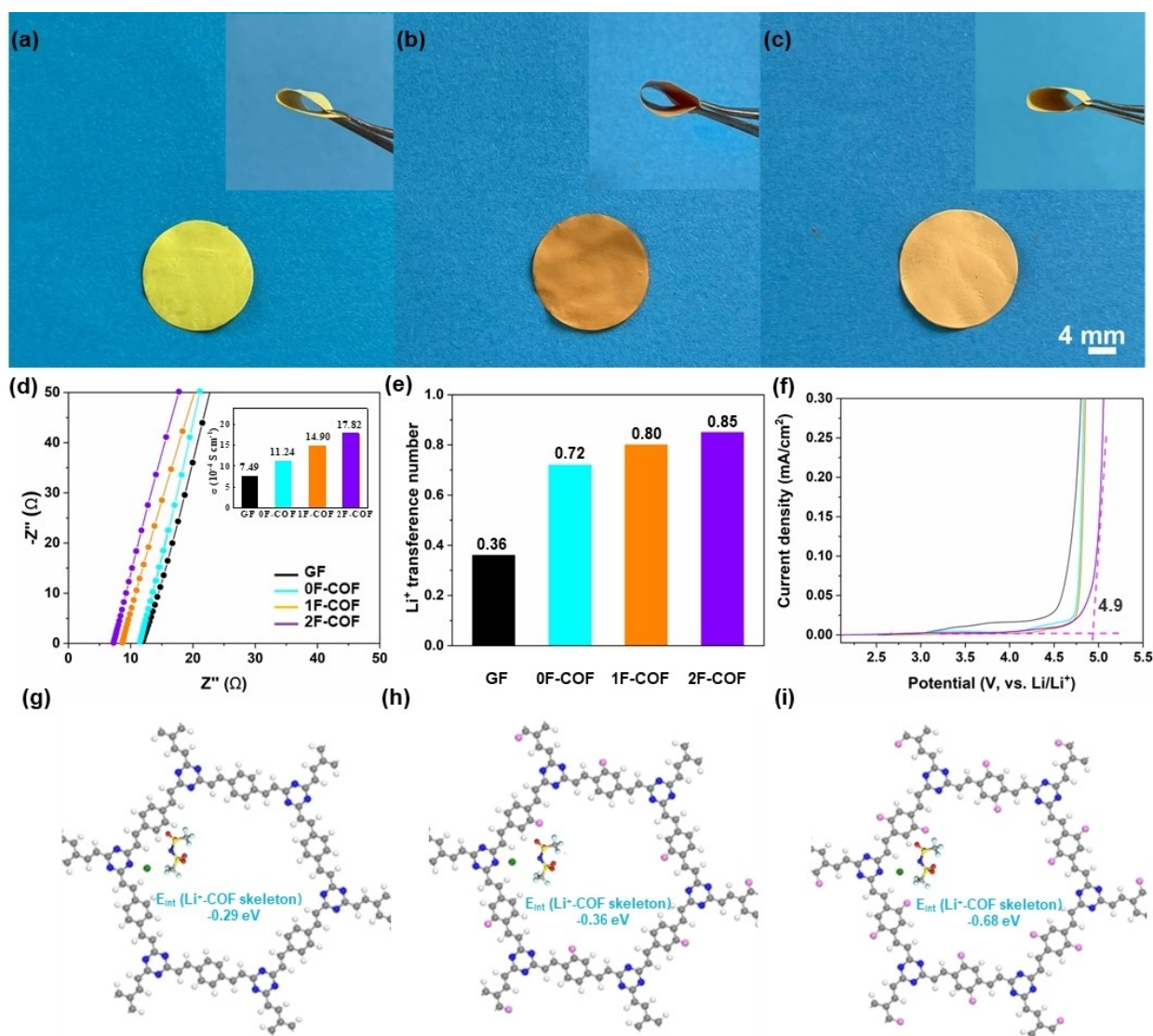


Figure 2. (a)–(c) Digital images of the EL-COF membranes before/after bending deformation (inset): (a) 0F-COF, (b) 1F-COF, and (c) 2F-COF. (d) Nyquist plots of the EL-COF membranes at room temperature (Inset: ionic conductivity). (e) Li^+ transference number of the EL-COF membranes. (f) Linear sweep voltammetry (LSV) curves of the EL-COF membranes at room temperature. (g)–(i) Intermolecular interactions between LiTFSI and EL-COF membranes: (g) 0F-COF, (h) 1F-COF, and (i) 2F-COF.

were attributed to the electronegativity-rich 1D channels which enabled ion-dipole interaction with Li^+ .

This advantageous effect of the EL-COF membranes was theoretically verified using density functional theory (DFT) calculation, with a focus on adsorption energy of Li^+ to COF skeletons. The calculated adsorption energies of 0F-COF, 1F-COF, and 2F-COF were -0.29 , -0.36 , and -0.68 eV, respectively (Figure 2g–2i). The enhanced adsorption energies of the 2F-COF were attributed to the electronegativity-rich sites derived from F atoms, which could preferentially attract Li^+ , thereby increasing the number of free Li^+ and guiding uniform Li^+ flux within the 1D channels.

It is known that Li^+ conductivity ($=$ ionic conductivity $\times t_+$) plays a more significant role in affecting practical cell performance compared to ionic conductivity. Therefore, we estimated the Li^+ conductivity using the results of the ionic conductivity and t_+ (Figure 2d, inset and Figure S11b–c). Among the membranes, the 2F-COF membrane exhibited superior Li^+ conductivity, underscoring the beneficial effect of the electronegativity-rich 1D channels. The ionic conductivity and Li^+ conductivity of the 2F-COF exceeded those of previously reported COF-based ion conductors (Table S2).

The electrochemical stability window of the EL-COF membranes was investigated using linear sweep voltammetry (LSV) analysis (Figure 2f and Figure S11d). The EL-COF membranes were electrochemically stable up to 4.2 V. Particularly, the 2F-COF exhibited the highest oxidation stability (≈ 4.9 V vs Li/Li^+), indicating its potential use in high-voltage cells.

The effect of the EL-COF membranes on the Coulombic Efficiency (CE) of Li during plating/stripping cycling was investigated using Li/Cu asymmetric cells (Figure 3a). The GF membrane exhibited an initial CE of approximately 70 %, which declined rapidly after 20 cycles, indicating its irreversible capacity loss owing to the uneven Li deposition and uncontrollable lithium dendrite growth. In contrast, the COF membranes exhibited significantly improved cycling performance and CE, which was more pronounced in the 2F-COF (CE ≈ 94 % after 100 cycles).

The initial Li plating profiles revealed that the GF membrane exhibited an overpotential of 104 mV, which was considerably higher than those of the 0F-COF (77 mV), 1F-COF (60 mV), and 2F-COF (42 mV; Figure 3b). The lowest overpotential value of the 2F-COF indicated that it exhibited the smallest nucleation barrier, which contributed to the facilitation of Li^+ migration through the 2F-COF. In addition, the EL-COF membranes exhibited lower voltage polarization than the GF membrane with an increase in the cycling numbers (Figure S13). The 2F-COF membrane maintained its voltage of approximately 35 mV, demonstrating the advantageous effect of its electronegativity-rich 1D channels.

Based on the above-described results of Li/Cu asymmetric cells, we investigated the Li plating/stripping cyclability of Li/Li symmetric cells assembled with the EL-COF membranes. The GF and PTFE membrane exhibited unstable Li plating/stripping voltage profiles with an in-

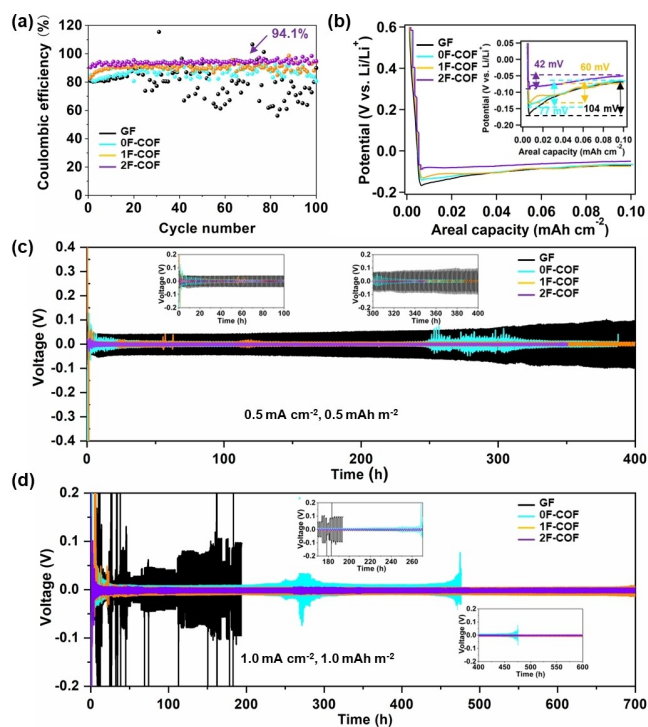


Figure 3. (a) Coulombic efficiency of Li//Cu asymmetric cells at a current density of 0.1 mA cm^{-2} with plating/stripping capacity of 0.1 mAh cm^{-2} . (b) Comparison of Li nucleation and voltage hysteresis variation at 0.1 mA cm^{-2} (inset: a magnified view in the potential range below 0.0 V). Li stripping/ plating behavior of Li//Li symmetric cells at a current density of (c) 0.5 mA cm^{-2} for 0.5 mAh cm^{-2} and (d) 1.0 mA cm^{-2} for 1.0 mAh cm^{-2} with GF (black), 0F-COF (cyan), 1F-COF (orange), and 2F-COF (purple) (inset: the magnified views in the different cycling time).

crease in the number of cycles at a current density of 0.5 mA cm^{-2} and a capacity of 0.5 mAh cm^{-2} (Figure 3c and S14), even at a larger current density of 1 mA cm^{-2} and a capacity of 1 mAh cm^{-2} (Figure 3d). In addition, the cell with the GF membrane exhibited a short-circuit failure after 15 h at a current density of 1 mA cm^{-2} and a capacity of 1 mAh cm^{-2} . This poor cyclability was attributed to the uneven and irregular Li^+ flux on Li metals, which enabled the growth of Li dendrites. In contrast, the EL-COF membrane exhibited significantly improved Li plating/stripping cyclability and overpotential in the order of $0\text{F-COF} < 1\text{F-COF} < 2\text{F-COF}$. The well-defined 1D channels of the EL-COF membranes enabled uniform Li^+ flux towards the Li metals. Moreover, owing to the electronegativity-rich sites, the EL-COF membranes could guide Li^+ migration within the 1D channels, resulting in faster Li^+ movement. These results verified the viable role of the electronegativity-rich 1D channels of the EL-COF membranes in enabling facile and uniform Li^+ flux towards the Li metals, which played a viable role in stabilizing the Li plating/stripping cyclability. This improvement in the cyclability was verified using electrochemical impedance spectroscopy (EIS) analysis (Figure S15). The 2F-COF exhibited significantly suppressed the increase in the cell resistance compared to the other samples, demonstrating its advantageous effect on the

Li metal stabilization. Particularly, the SEI resistance (R_{SEI}) of the membranes decreased in the order of GF > 0F-COF > 1F-COF > 2F-COF, indicating that the 2F-COF contributed to the formation of a stable SEI layer, which enable facile Li^+ migration.

To further elucidate the aforementioned stable Li plating/stripping cyclability of the EL-COF membranes, the Li metals (after 100 cycles) from the Li/Li symmetric cells cycled at a current density of 0.5 mA cm^{-2} were analyzed. Random and uneven Li dendrites were formed in the cycled Li metal assembled with the GF membrane (Figure S16). In contrast, the surface of the cycled Li metal coupled with the EL-COF membranes exhibited a smooth and flat surface morphology, which was more pronounced in the 2F-COF.

This difference in the morphology of the cycled Li metal was verified by analyzing the SEI layers using X-ray photoelectron spectroscopy (XPS) analysis. The C–C, C–O, C=O, and CO_3^{2-} peaks observed in the C 1s spectrum were assigned to ROCO_2Li , RCOOLi , and Li_2CO_3 , respectively (Figure S17). Organic components of the SEI, which are composed of ROCO_2Li and RCOOLi , are known to be mechanically flexible, thus alleviating volume changes during Li plating/stripping. The LiF, which is a major inorganic component of the SEI, tends to increase in the order of 0F-COF < 1F-COF < 2F-COF (Figure 4a–4b), indicating the improved structural stability of the SEI. In addition, the Li_3N content in the SEI was increased in the EL-COF membranes (particularly in 2F-COF). Considering that Li_3N is known to exhibit a high ionic conductivity ($\approx 10^{-3} \text{ S cm}^{-2}$), the higher Li_3N content in the SEI facilitated Li^+ migration across the SEI, beneficially contributing to reliable Li plating/stripping behavior. To better elucidate the advantageous effect of the 2F-COF membrane on the Li plating/stripping cycling behavior, we conducted in situ Raman and FT-IR spectroscopy characterization. The time-resolved contour map of the in situ Raman and the FT-IR spectra of the 2F-COF membrane were collected during the charging/discharging process. The characteristic Raman peaks (Figure 4c) were obviously observed, exhibiting the strong interaction between the 2F-COF and Li metal. In addition, the characteristic FT-IR peak of the C–F bond was detected in the 2F-COF (Figure 4d), demonstrating the viable role of the electronegative channels of the 2F-COF.

This structural characterization of the cycled Li metals was consistent with the Li plating/stripping cycling behavior described above, demonstrating the effectiveness of 2F-COF in stabilizing the Li metal owing to its electronegativity-rich 1D channels, which enabled uniform and facile Li^+ flux towards the Li metal.

The electrochemical performance of the EL-COF membranes was investigated using a Li (thickness = $450 \mu\text{m}$) || LiFePO_4 (LFP) (theoretical areal capacity = $0.425 \text{ mAh cm}^{-2}$) cell (CR2032-type) at room temperature. The cyclic voltammetry (CV) profiles of the cells were measured from 2.4 V to 4.2 V at a scan rate of 0.1 mV s^{-1} . The characteristic peaks assigned to cathodic and anodic reactions of LFP in the cathodes of the all cells were observed with an increase in the number of cycles (Figure 5a and Figure S18). These CV results were consistent with the

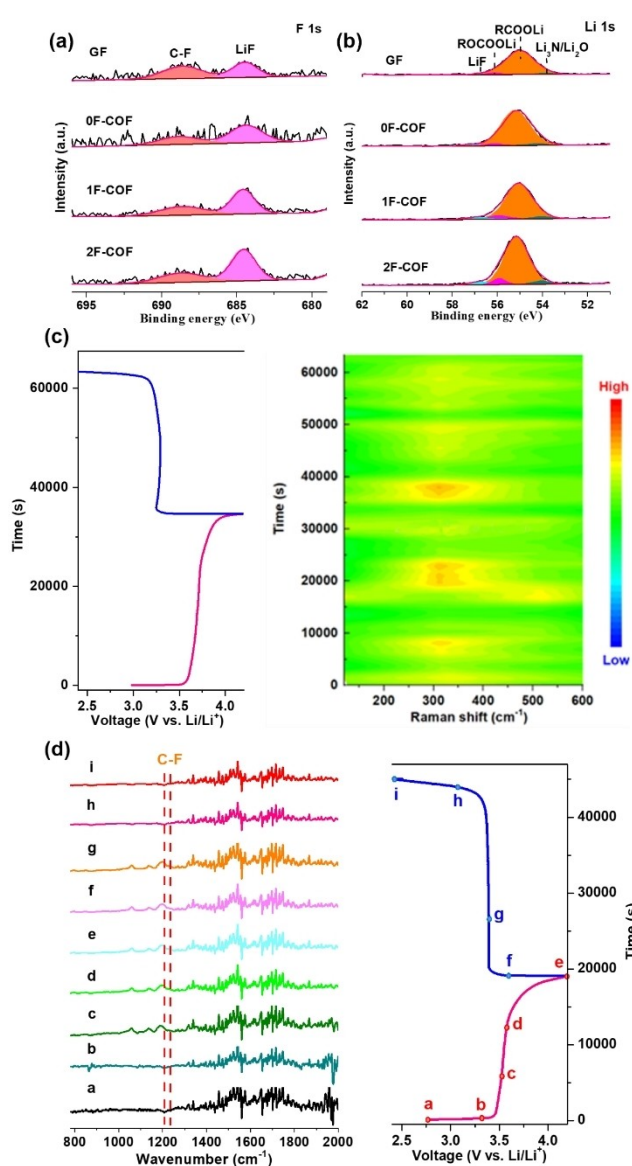


Figure 4. High-resolution XPS spectra of (a) F 1s and (b) Li 1s. (c) In situ time-resolved Raman and (d) FT-IR spectra obtained during discharging processes with Li/Li cell using 2F-COF separators. The blue and red curves represent the discharging processes.

charge/discharge voltage profiles shown in Figure 5c and Figure S19.

The cycling retention of the cells was examined at a current density of 0.1 C (Figure 5b and S20). The capacity of the cell with the GF membrane declined rapidly after 60 cycles, resulting in a capacity retention of 66 % after 100 cycles. Meanwhile, the 0F-COF exhibited improved capacity retention (88 % after 100 cycles) compared to the GF and PTFE membrane. In contrast, the 1F-COF and 2F-COF membranes exhibited a high capacity retention of 99 % after 100 cycles, along with stable voltage profiles. To further elucidate this superior cyclability of the 2F-COF, we examined the surface of the cycled Li metal anodes (Figure 5d). The cycled Li metal anode assembled with the 2F-COF membrane exhibited a uniform and smooth surface

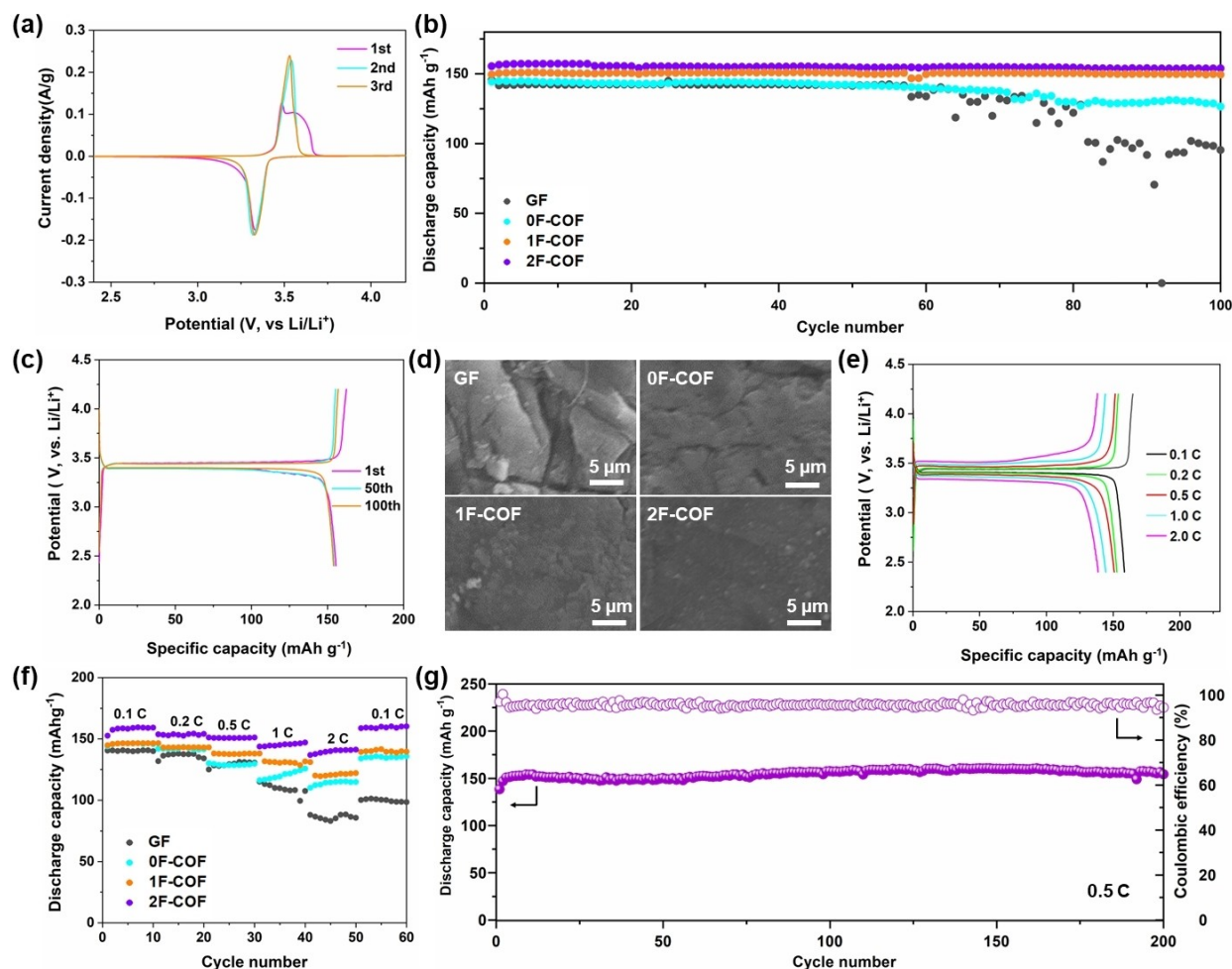


Figure 5. (a) CV curves of the Li || LFP cells with 2F-COF at a scan rate of 0.1 mV s^{-1} . (b) Cycling performance of the Li || LFP cells with GF, 0F-COF, 1F-COF, and 2F-COF at 0.1 C . (c) Discharge/charge voltage profiles of the Li || LFP cells with GF and 2F-COF at 0.1 C . (d) Surface FE-SEM images of the cycled Li metal anodes after 100 cycles. (e) Discharge and charge voltage profiles of the Li || LFP cells with 2F-COF at different current densities. (f) Rate capability of the Li || LFP cells with GF, 0F-COF, 1F-COF, and 2F-COF. (g) Cycling performance and Coulombic efficiency of the Li || LFP cells with 2F-COF at 0.5 C .

compared to the other samples. This result indicates that uniform and facile Li^+ flux through the 2F-COF could enable stable Li plating/stripping on the Li metal anode. In addition to its superior cyclability, the 2F-COF membrane exhibited the highest rate capability (Figure 5e and 5f).

The cell achieved a reliable cycling retention even at a faster rate of 0.5 C owing to the aforementioned Li metal stabilization and fast Li^+ flux enabled by the 2F-COF (Figure 5g). This cycling result of the 2F-COF outperforms those of previously reported COF-based ion conductors (Table S3), underscoring the rational design of the 2F-COF, which is featured with electronegativity-rich 1D channels.

Conclusion

In summary, we presented olefin-linked COFs with electronegative 1D channels as a selective ion-transport strategy to enable stable Li plating/stripping on Li metal anodes. To

this end, triazine rings and fluorine atoms were introduced into the COF skeletons to enrich the electronegativity in the 1D channels, thereby enhancing the dissociation of Li salts and guiding uniform Li^+ flux within the channels. To regulate the electronegativity of the 1D channels, a series of COFs with different numbers of fluorine atoms in the olefin linkage were synthesized. Among several (electrolyte-impregnated) COF membranes explored, the 2F-COF membrane, which exhibited the highest electronegativity, exhibited a high t_{Li^+} of 0.85 and high ionic conductivity of 1.78 mS cm^{-1} , demonstrating the promotion of Li^+ transport via the 1D channels. Owing to these advantageous effects, the 2F-COF achieved the reliable Li plating/stripping behavior and the long cycling retention of Li metal cells compared to previously reported COF-based ion conductors. The ion-selective COFs with electronegative channels are promising as a class of cationic highway that can enable uniform and facile Li^+ transport towards Li metal anodes

and can be extended as a platform technology to other metal batteries (such as sodium, zinc, and magnesium).

Acknowledgements

This work was supported by the financial support from the National Natural Science Foundation of China (52103277), the Program for Science & Technology Innovation Talents in Universities of Henan Province (23HASTIT015), Key Projects of Science and Technology of Henan Province (222102240098), Key Scientific Research Project of Henan Universities (21A150061), the Basic Science Research Program (2021R1A2B5B03001615) through the National Research Foundation of Korea (NRF) funded by the Ministry of Science, ICT and future Planning. This work was also supported by the Technology Innovation Program (20012216) funded by the Ministry of Trade, Industry & Energy (MOTIE, Korea).

Conflict of Interest

The authors declare no conflict of interest.

Data Availability Statement

The data that support the findings of this study are available in the supplementary material of this article.

Keywords: Cationic Membranes • Covalent Organic Frameworks • Electronegative Channels • Lithium Batteries • Olefin Linkage

- [1] X.-B. Cheng, R. Zhang, C.-Z. Zhao, Q. Zhang, *Chem. Rev.* **2017**, *117*, 10403–10473.
- [2] P. Bai, X. Ji, J. Zhang, W. Zhang, S. Hou, H. Su, M. Li, T. Deng, L. Cao, S. Liu, X. He, Y. Xu, C. Wang, *Angew. Chem. Int. Ed.* **2022**, *61*, e202202731.
- [3] Z. Lin, T. Liu, X. Ai, C. Liang, *Nat. Commun.* **2018**, *9*, 5262.
- [4] D. Lin, Y. Liu, Y. Cui, *Nat. Nanotechnol.* **2017**, *12*, 194–206.
- [5] J. Wang, L. Li, H. Hu, H. Hu, Q. Guan, M. Huang, L. Jia, H. Adenusi, K. V. Tian, J. Zhang, S. Passerini, H. Lin, *ACS Nano* **2022**, *16*, 17729–17760.
- [6] M. Huang, Z. Yao, Q. Yang, C. Li, *Angew. Chem. Int. Ed.* **2021**, *60*, 14040–14050.
- [7] Y. Liu, Z. Tu, L. A. Archer, *Nat. Mater.* **2014**, *13*, 961–969.
- [8] X.-B. Cheng, R. Zhang, C.-Z. Zhao, F. Wei, J.-G. Zhang, Q. Zhang, *Adv. Sci.* **2016**, *3*, 1500213.
- [9] M. Asadi, B. Sayahpour, P. Abbasi, A. T. Ngo, K. Karis, J. R. Jokisaari, C. Liu, B. Narayanan, M. Gerard, P. Yasaei, X. Hu, A. Mukherjee, K. C. Lau, R. S. Assary, F. Khalili-Araghi, R. F. Klie, L. A. Curtiss, A. Salehi-Khojin, *Nature* **2018**, *555*, 502–506.
- [10] J. Wang, H. Hu, J. Zhang, L. Li, L. Jia, Q. Guan, H. Hu, H. Liu, Y. Jia, Q. Zhuang, S. Cheng, M. Huang, H. Lin, *Energy Storage Mater.* **2022**, *52*, 210–219.
- [11] J. Zhang, R. He, Q. Zhuang, X. Ma, C. You, Q. Hao, L. Li, S. Cheng, L. Lei, B. Deng, X. Li, H. Lin, J. Wang, *Adv. Sci.* **2022**, *9*, 2202244.
- [12] X. Chen, X. Shen, B. Li, H.-J. Peng, X.-B. Cheng, B.-Q. Li, X.-Q. Zhang, J.-Q. Huang, Q. Zhang, *Angew. Chem. Int. Ed.* **2018**, *57*, 734–737.
- [13] Y. Jie, X. Liu, Z. Lei, S. Wang, Y. Chen, F. Huang, R. Cao, G. Zhang, S. Jiao, *Angew. Chem. Int. Ed.* **2020**, *59*, 3505–3510.
- [14] H. Yang, X. Lin, C. Wei, J. Feng, X. Tian, *Small* **2021**, *18*, 2104264.
- [15] C. Jiang, Q. Jia, M. Tang, K. Fan, Y. Chen, M. Sun, S. Xu, Y. Wu, C. Zhang, J. Ma, C. Wang, W. Hu, *Angew. Chem. Int. Ed.* **2021**, *60*, 10871–10879.
- [16] W. Zhao, L. Zou, J. Zheng, H. Jia, J. Song, M. H. Engelhard, C. Wang, W. Xu, Y. Yang, J.-G. Zhang, *ChemSusChem* **2018**, *11*, 2211–2220.
- [17] H. Cavers, P. Molaiyan, M. Abdollahifar, U. Lassi, A. Kwade, *Adv. Energy Mater.* **2022**, *12*, 2200147.
- [18] M. Li, Z. Zhang, Y. Yin, W. Guo, Y. Bai, F. Zhang, B. Zhao, F. Shen, X. Han, *ACS Appl. Mater. Interfaces* **2020**, *12*, 3610–3616.
- [19] W. Na, K. H. Koh, A. S. Lee, S. Cho, B. Ok, S. Hwang, J. H. Lee, C. M. Koo, *J. Membr. Sci.* **2019**, *573*, 621.
- [20] L. Tan, Y. Sun, C. Wei, Y. Tao, Y. Tian, Y. An, Y. Zhang, S. Xiong, J. Feng, *Small* **2021**, *17*, 2007717.
- [21] Z. Chang, Y. Qiao, H. Yang, X. Cao, X. Zhu, P. He, H. Zhou, *Angew. Chem. Int. Ed.* **2021**, *60*, 15572–15581.
- [22] Z. Chang, Y. Qiao, H. Yang, H. Deng, X. Zhu, P. He, H. Zhou, *Energy Environ. Sci.* **2020**, *13*, 4122–4131.
- [23] C. Wei, Y. Wang, Y. Zhang, L. Tan, Y. Qian, Y. Tao, S. Xiong, J. Feng, *Nano Res.* **2021**, *14*, 3576–3584.
- [24] Y. Yang, S. Yao, Z. Liang, Y. Wen, Z. Liu, Y. Wu, J. Liu, M. Zhu, *ACS Energy Lett.* **2022**, *7*, 885–896.
- [25] S. Yao, Y. Yang, Z. Liang, J. Chen, J. Ding, F. Li, J. Liu, L. Xi, M. Zhu, J. Liu, *Adv. Funct. Mater.* **2023**, *33*, 2212466.
- [26] a) K. Jeong, S. Park, G. Y. Jung, S. H. Kim, Y.-H. Lee, S. K. Kwak, S.-Y. Lee, *J. Am. Chem. Soc.* **2019**, *141*, 5880–5885; b) M. Tang, C. Jiang, S. Liu, X. Li, Y. Chen, Y. Wu, J. Ma, C. Wang, *Energy Storage Mater.* **2020**, *27*, 35.
- [27] a) K. Zhang, X. Li, L. Ma, F. Chen, Z. Chen, Y. Yuan, Y. Zhao, J. Yang, J. Liu, K. Xie, K. P. Loh, *ACS Nano* **2023**, *17*, 2901–2911; b) X. Li, Q. Hou, W. Huang, H.-S. Xu, X. Wang, W. Yu, R. Li, K. Zhang, L. Wang, Z. Chen, K. Xie, K. P. Loh, *ACS Energy Lett.* **2020**, *5*, 3498–3506.
- [28] J. Zou, K. Fan, Y. Chen, W. Hu, C. Wang, *Coord. Chem. Rev.* **2022**, *458*, 214431.
- [29] a) F. Meng, S. Bi, Z. Sun, D. Wu, F. Zhang, *Angew. Chem. Int. Ed.* **2022**, *61*, e202210447; b) S. Bi, Z. Zhang, F. Meng, D. Wu, J.-S. Chen, F. Zhang, *Angew. Chem. Int. Ed.* **2022**, *61*, e202111627.
- [30] a) S. Xu, G. Wang, B. P. Biswal, M. Addicoat, S. Paasch, W. Sheng, X. Zhuang, E. Brunner, T. Heine, R. Berger, X. Feng, *Angew. Chem. Int. Ed.* **2019**, *58*, 849–853; b) S. Li, R. Ma, S. Xu, T. Zheng, G. Fu, Y. Wu, Z. Liao, Y. Kuang, Y. Hou, D. Wang, P. S. Petkov, K. Simeonova, X. Feng, L.-Z. Wu, X.-Bi. Li, T. Zhang, *J. Am. Chem. Soc.* **2022**, *144*, 13953–13960.
- [31] S. Bi, P. Thiruvengadam, S. Wei, W. Zhang, F. Zhang, L. Gao, J. Xu, D. Wu, J.-S. Chen, F. Zhang, *J. Am. Chem. Soc.* **2020**, *142*, 11893–11900.
- [32] M. Wang, P. Zhang, X. Liang, J. Zhao, Y. Liu, Y. Cao, H. Wang, Y. Chen, Z. Zhang, F. Pan, Z. Zhang, Z. Jiang, *Nat. Sustainability* **2022**, *5*, 518–526.
- [33] a) Z. Wang, Y. Yang, Z. Zhao, P. Zhang, Y. Zhang, J. Liu, S. Ma, P. Cheng, Y. Chen, Z. Zhang, *Nat. Commun.* **2021**, *12*, 1982; b) Y.-J. Li, W.-R. Cui, Q.-Q. Jiang, Q. Wu, R.-P. Liang, Q.-X. Luo, J.-D. Qiu, *Nat. Commun.* **2021**, *12*, 4735.
- [34] X. Guan, F. Chen, S. Qiu, Q. Fang, *Angew. Chem. Int. Ed.* **2023**, *62*, e202213203.
- [35] W. Weng, J. Guo, *Nat. Commun.* **2022**, *13*, 5768.

- [36] G. Xing, J. Liu, Y. Zhou, S. Fu, J.-J. Zheng, X. Su, X. Gao, O. Terasaki, M. Bonn, H. I. Wang, L. Chen, *J. Am. Chem. Soc.* **2023**, *145*, 8979–8987.
- [37] C. Lin, L. Sun, X. Meng, X. Yuan, C.-X. Cui, H. Qiao, P. Chen, S. Cui, L. Zhai, L. Mi, *Angew. Chem. Int. Ed.* **2022**, *61*, e202211601.
- [38] Y. Yang, X. Chu, H.-Y. Zhang, R. Zhang, Y.-H. Liu, F.-M. Zhang, M. Lu, Z.-D. Yang, Y.-Q. Lan, *Nat. Commun.* **2023**, *14*, 593.
- [39] K. Geng, T. He, R. Liu, S. Dalapati, K. T. Tan, Z. Li, S. Tao, Y. Gong, Q. Jiang, D. Jiang, *Chem. Rev.* **2020**, *120*, 8814–8933.
- [40] Z. Lei, Q. Yang, Y. Xu, S. Guo, W. Sun, H. Liu, L.-P. Lv, Y. Zhang, Y. Wang, *Nat. Commun.* **2018**, *9*, 576.
- [41] H. Lyu, H. Li, N. Hanikel, K. Wang, O. M. Yaghi, *J. Am. Chem. Soc.* **2022**, *144*, 12989–12995.
- [42] H. Yang, J. Xu, H. Cao, J. Wu, D. Zhao, *Nat. Commun.* **2023**, *14*, 2726.
- [43] Z. Mu, Y. Zhu, Y. Zhang, A. Dong, C. Xing, Z. Niu, B. Wang, X. Feng, *Angew. Chem. Int. Ed.* **2023**, *62*, e202300373.
- [44] B. Hu, J. Xu, Z. Fan, C. Xu, S. Han, J. Zhang, L. Ma, B. Ding, Z. Zhuang, Q. Kang, X. Zhang, *Adv. Energy Mater.* **2023**, *13*, 2203540.
- [45] C. Wei, L. Tan, Y. Zhang, K. Zhang, B. Xi, S. Xiong, J. Feng, Y. Qian, *ACS Nano* **2021**, *15*, 12741–12767.
- [46] M. J. Lee, J. Han, K. Lee, Y. J. Lee, B. G. Kim, K.-N. Jung, B. J. Kim, S. W. Lee, *Nature* **2022**, *601*, 217–222.
- [47] C. Fu, Y. Ma, S. Lou, C. Cui, L. Xiang, W. Zhao, P. Zuo, J. Wang, Y. Gao, G. Yin, *J. Mater. Chem. A* **2020**, *8*, 2066–2073.
- [48] F. Fu, Y. Liu, C. Sun, L. Cong, Y. Liu, L. Sun, H. Xie, *Energy Environ. Mater.* **2023**, *6*, e12367.
- [49] H. Gao, L. Xue, S. Xin, K. Park, J. B. Goodenough, *Angew. Chem. Int. Ed.* **2017**, *56*, 5541–5545.

Manuscript received: May 29, 2023

Accepted manuscript online: July 24, 2023

Version of record online: August 4, 2023